







## Observation of weak localization in dual-gated bilayer MoS<sub>2</sub>

Tingyu Qu <sup>1,2,\*</sup> Michele Masseroni <sup>3</sup> Takashi Taniguchi <sup>3</sup> Kenji Watanabe <sup>3</sup> Barbaros Özyilmaz<sup>1,2</sup>  
Thomas Ihn <sup>4</sup> and Klaus Ensslin <sup>4</sup>

<sup>1</sup>*NUS Graduate School, Integrative Sciences and Engineering Programme, National University of Singapore, Singapore*

<sup>2</sup>*Department of Physics, National University of Singapore, Singapore*

<sup>3</sup>*National Institute for Materials Science, 1-1 Namiki, Tsukuba 305-0044, Japan*

<sup>4</sup>*Solid State Physics Laboratory, ETH Zürich, 8093 Zürich, Switzerland*



(Received 23 September 2023; accepted 31 January 2024; published 28 February 2024)

We investigate the magnetoresistance of a dual-gated bilayer MoS<sub>2</sub> encapsulated by hexagonal boron nitride. At low magnetic fields ( $|B| < 0.5$  T), we observe a negative magnetoresistance, which we identify as the weak localization effect. We determine both the phase coherence length and mean free path as a function of electron density and displacement field. Both characteristic lengths show a similar monotonic increase with electron density, while they are not affected by the displacement field. We further investigate the dephasing mechanism by measuring the temperature dependence of the phase coherence length. Our results suggest that when only the lower spin-orbit split bands ( $K \uparrow, K' \downarrow$ ) contribute to transport is Coulomb scattering the dominant source of decoherence, while intervalley scattering seems not to play a relevant role in this regime. This observation is consistent with the picture of spin-polarized valleys (spin-valley locking), where the intrinsic spin-orbit coupling protects the spin states, rather than introducing an additional dephasing mechanism as in other materials.

DOI: [10.1103/PhysRevResearch.6.013216](https://doi.org/10.1103/PhysRevResearch.6.013216)

### I. INTRODUCTION

In the diffusive transport regime, the magnetoresistance (MR) of electronic systems deviates from Boltzmann theory and displays an enhancement at zero field [1]. This magnetoresistance peak is a quantum effect that originates from time-reversed paths of electrons interfering constructively in scattering loops. This effect is referred to as weak localization (WL) [2].

Transition metal dichalcogenide (TMDC) monolayers have no inversion symmetry in the lattice sites [3,4]. Furthermore, spin-orbit coupling is particularly strong in the valence band, but also present in the conduction band. For example, molybdenum disulfide (MoS<sub>2</sub>) hosts an intrinsic spin-orbit coupling (SOC) that behaves as an out-of-plane Zeeman field and pins the two spins with opposite directions in  $K$  and  $K'$  valleys [5,6]. In contrast to other materials (e.g., Bernal stacked bilayer graphene, bilayer or trilayer MoS<sub>2</sub>), the  $K$ -valley electrons of different layers behave as independent systems owing to the weak interlayer coupling [7,8].

In the presence of SOC effects, the spin of an electron rotates as it is scattered between self-crossing paths, yielding a destructive interference and a lower zero-field resistivity called weak antilocalization (WAL) [9,10]. The study of

W(A)L in two-dimensional (2D) systems in a magnetic field perpendicular to the 2D plane allows us to assess some fundamental characteristics of the charge carriers, such as phase coherence and scattering rates as well as the strength of SOC [11–14].

Previous investigations about the W(A)L in monolayer [15], bilayer [16], and few-layer MoS<sub>2</sub> samples [17,18] lack a dual-gated device structure. In addition, the influence of carrier population of different spin-split bands in the presence of W(A)L has not been presented yet. Also, in light of the limitation that the Hikami-Larkin-Nagaoka (HLN) model [9] is insufficient to allow interpretation of the spin splitting due to the intrinsic SOC in TMDC [12], caution might be warranted when extracting spin relaxation lengths from the spin-orbit scattering in the HLN model.

In this paper, we show that electron transport in a dual-gated bilayer MoS<sub>2</sub> can be entirely described by WL, without taking into account spin-orbit coupling. We observe a pronounced WL peak when the electrons populate a single layer (top layer), while it is not present when both layers are occupied. We do not observe WAL, suggesting a minor effect of SOC on quantum interference. We simplify the fitting model by neglecting the SOC term in the HLN model and describe our data with only two parameters, namely, the phase coherence length and elastic mean free path. We determine the mean free path from the zero-field conductivity and extract the phase coherence length by fitting the weak localization peak, taking the phase coherence length as the only fitting parameter. Based on our evaluation, the phase coherence length at a temperature of 1.3 K exceeds 100 nm for densities  $>7 \times 10^{12}$  cm<sup>-2</sup> and it shows a linear dependence on the density. On the other hand, when tuning the displacements

\*ty.qu@nus.edu.sg

Published by the American Physical Society under the terms of the [Creative Commons Attribution 4.0 International](https://creativecommons.org/licenses/by/4.0/) license. Further distribution of this work must maintain attribution to the author(s) and the published article's title, journal citation, and DOI.

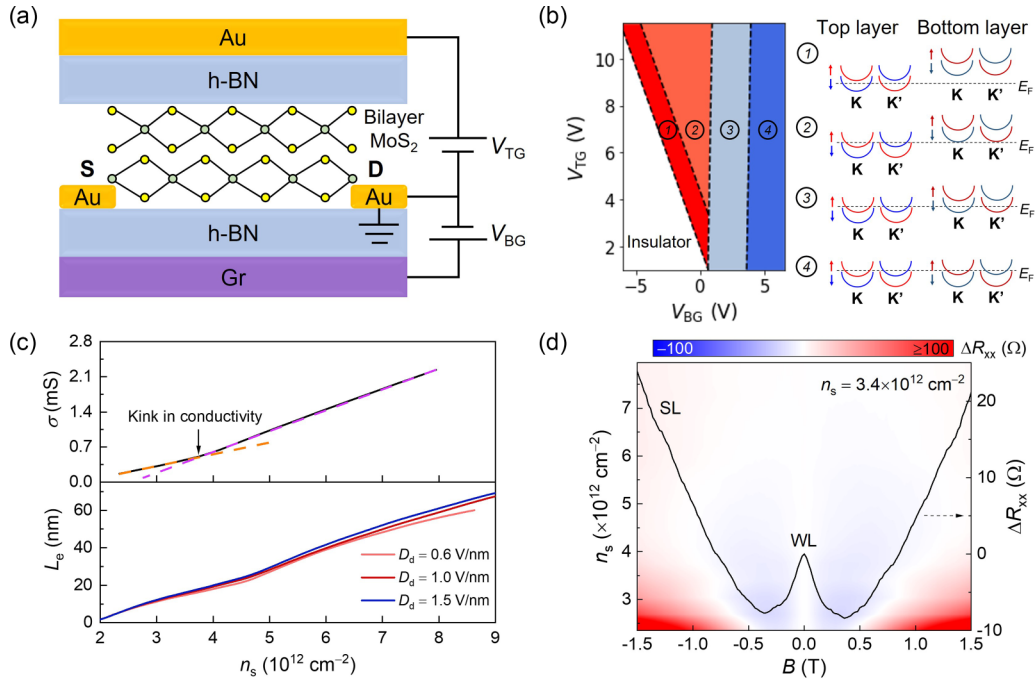


FIG. 1. (a) Device schematics. The bilayer MoS<sub>2</sub> is encapsulated between two h-BN flakes, with metallic contacts (Au) as the source/drain (S/D) and dual gates (Au as top gate and graphite as bottom gate). (b) Phase diagram for the population of the carriers in different bands as a function of top and bottom gates. The diagram is reconstructed from the measurement of the magnetoresistance at  $T = 1.3$  K and  $B = 7$  T presented in Ref. [19]. The white-color regime refers to the insulating state. The colored regimes (from left to right, labeled by 1–4) indicate the population of the lower band in the top layer, upper band in the top layer, lower band in the bottom layer, and upper band in the bottom layer, respectively. (c)  $\sigma_{xx} - n_s$  (top subfigure) and  $L_e - n_s$  (bottom subfigure) curves at  $T = 1.3$  K and  $B = 0$  T, based on the forms  $\sigma = n_s e \mu$  and  $L_e = \sigma \hbar / e^2 \sqrt{4\pi / (g_v n_s)}$  (where  $g_v = 2$  is the valley degeneracy in each spin-valley locked band). A kink in  $\sigma_{xx} - n_s$  can be identified by the intersection of the two linear fits. The onset of mobility in the upper spin-split band correspond to  $3.8 \times 10^{12} \text{ cm}^{-2}$ . (d) Normalized MR as a function of  $B$  and  $n_s$  populated in the first layer at  $T = 1.3$  K. The overlaid linecut shows the normalized MR at  $n_s = 3.3 \times 10^{12} \text{ cm}^{-2}$ .

field while keeping the density constant, we do not observe any evident dependence. The temperature dependence of the phase coherence length shows  $T^{-\alpha}$  with  $\alpha \approx 0.5$  in the single-band regime. All these observations hint towards Coulomb interaction as the main dephasing mechanism and a spin relaxation length much longer than the phase coherence length in 2D MoS<sub>2</sub>.

## II. RESULTS AND DISCUSSION

Our device schematics is shown in Fig. 1(a). The bilayer MoS<sub>2</sub> sample is encapsulated by two hexagonal boron nitride flakes (h-BN) as the dielectric layers, which allows us to tune the total carrier density ( $n_s$ ) from a top gate (Au) and a bottom gate (graphite) by the parallel-capacitance model with the form of  $n_s = \frac{1}{e} (C_B V_{BG} + C_T V_{TG})$ , where  $C_B = \epsilon_0 \epsilon / d_B$  and  $C_T = \epsilon_0 \epsilon / d_T$  refer to the capacitances of the bottom BN and top BN layers, respectively ( $\epsilon_0$  and  $\epsilon$  are the vacuum permittivity and the dielectric constant  $\sim 3.3$ , respectively;  $d_B$  and  $d_T$  refer to the thicknesses of the bottom and top BN layers);  $V_{BG}$  and  $V_{TG}$  refer to the back-gate and top-gate voltages, respectively. The details of the device fabrication and measurement are shown in Appendix A. Each MoS<sub>2</sub> layer contributes with two spin-split bands, where the spin and valley are locked because of the intrinsic spin-orbit coupling [5]. As reported in our previous work [19], the onset of the population in each spin-split band is determined from Shubnikov–de Haas (SdH)

oscillation frequencies. To highlight the population of the carriers in each band as a function of both gates, a schematic phase diagram is presented in Fig. 1(b). The four colored regimes (from left to right) indicate the population of the carriers from the top layer (labeled by 1 and 2) to the bottom layer (labeled by 3 and 4) as the dual gating effect increases.

The carrier density dependence of the conductivity ( $\sigma$ ) and mean free path ( $L_e$ ) at zero field is shown in Fig. 1(c). The longitudinal conductivity  $\sigma_{xx}$  is given by  $\sigma_{xx} = \rho_{xx} / (\rho_{xx}^2 + \rho_{xy}^2)$ , where  $\rho_{xx}$  and  $\rho_{xy}$  are the measured longitudinal and Hall resistivities, respectively (see more details in Appendix B). We extract  $\sigma_{xx} \approx 0.17$  mS (over four times of  $e^2/h$ ) at the lowest carrier density we could reach for the WL analysis ( $n_s = 2.3 \times 10^{12} \text{ cm}^{-2}$ ). An approximate linear correlation between  $\sigma_{xx}$  and  $n_s$  exists before and after a kink point (at about  $n_s = 3.8 \times 10^{12} \text{ cm}^{-2}$ ). The kink refers to the onset of mobility ( $\mu$ ) in the upper band, which arises from the onset of the population of carriers. The  $L_e - n_s$  curves at various displacement fields ( $D_d$ ) show nearly identical patterns that can be described by a power law. Therefore, we conclude that the mean free path does not depend on the displacement field. Figure 1(d) shows a map of the normalized magnetoresistance [ $\Delta \text{MR} = \text{MR}(B) - \text{MR}(B = 0 \text{ T})$ ] as a function of  $B$  and  $n_s$  in the regime where only one layer is populated. At base temperature, clear zero-field peaks in the MR are observed in the entire single-layer regime (from  $n_s = 2.3 \times 10^{12} \text{ cm}^{-2}$  to  $n_s = 8.0 \times 10^{12} \text{ cm}^{-2}$ ), demonstrating the relevance of the

quantum interference effect. The origin of the positive MR at large field in the single-band regime is discussed separately in our previous work [19].

We turn our attention to analysis of W(A)L. First, we present the HLN model that includes the phase coherence, spin orbit, and elastic scattering in the form [1,9,10]

$$\begin{aligned} \Delta\sigma(B) = & \frac{e^2}{2\pi h} \left[ \ln\left(\frac{B_\phi}{B}\right) - \Psi\left(\frac{1}{2} + \frac{B_\phi}{B}\right) \right] \\ & + \frac{e^2}{\pi h} \left[ \ln\left(\frac{B_{SO} + B_e}{B}\right) - \Psi\left(\frac{1}{2} + \frac{B_{SO} + B_e}{B}\right) \right] \\ & + \frac{3e^2}{2\pi h} \left[ -\ln\left(\frac{4/3B_{SO} + B_\phi}{B}\right) \right. \\ & \left. + \Psi\left(\frac{1}{2} + \frac{4/3B_{SO} + B_\phi}{B}\right) \right], \end{aligned}$$

where  $B_\phi$ ,  $B_{SO}$ ,  $B_e$  refer to the field scales for the phase coherence, spin-orbit coupling, and elastic scattering, respectively.  $\Delta\sigma(B) = \sigma(B) - \sigma(B = 0 \text{ T})$  represents the normalized conductivity in the unit of  $e^2/\pi h$ .  $\Psi$  is the digamma function.

To understand the role of SOC on WAL, we simulate the turnover from WL to WAL by varying  $B_{SO}$  based on the above HLN model. To satisfy the single-band structure required in the HLN model [12], we choose the density  $n_s = 3.3 \times 10^{12} \text{ cm}^{-2}$ , for which we experimentally establish that the carriers occupy only the lower spin-orbit split bands in the top layer. In the simulation, a turnover from WL to WAL appears only if the length scale satisfies  $L_{SO} < L_\phi$ , where  $L_{SO}$  and  $L_\phi$  are the spin relaxation length and phase coherence length, respectively (see Appendix B). However, in the experiment, we do not observe WAL throughout the entire tunable range of the carrier density (from  $2.3 \times 10^{12} \text{ cm}^{-2}$  to  $2.0 \times 10^{13} \text{ cm}^{-2}$ ). The crossover from WL to WAL was observed at high carrier densities ( $\sim 1.0 \times 10^{14} \text{ cm}^{-2}$ ) with an ionic liquid gate [18], and it was shown that the spin-orbit length diverges at densities lower than  $5.0 \times 10^{13} \text{ cm}^{-2}$  [18]. In our case, the absence of WAL implies  $L_{SO} > L_\phi$  and  $L_{SO} \gg L_e$ . Consequently, the values of  $L_{SO}$  deduced from WL are less reliable than those deduced from WAL [18]. Moreover, our observation suggests that the intrinsic SOC in MoS<sub>2</sub> has a minor consequence for quantum interference of conduction electrons, in agreement with the reported surprisingly long-lived and coherent spin dynamics in monolayer MoS<sub>2</sub> [20,21], and so it has little impact on the shape of the magnetoconductivity if  $L_{SO} \gg L_e$ ,  $L_\phi$  [2].

Therefore, we simplify the HLN model by leaving out the SOC term, which allows us to accurately evaluate  $L_\phi$ . By substituting  $B_\phi = \hbar/(4eL_\phi^2)$  and  $B_e = \hbar/(4eL_e^2)$ , we describe the WL only with  $L_\phi$  and  $L_e$  in the form

$$\begin{aligned} \Delta\sigma(B) = & N \frac{e^2}{\pi h} \left[ \Psi\left(\frac{1}{2} + \frac{\hbar}{4eBL_\phi^2}\right) - \Psi\left(\frac{1}{2} + \frac{\hbar}{4eBL_e^2}\right) \right. \\ & \left. + 2\ln\left(\frac{L_\phi}{L_e}\right) \right], \end{aligned}$$

where  $\Psi$  is the digamma function and  $N$  is a coefficient that implies the number of populated bands in the system. If the electrons are populated in the single band and the spin-orbit scattering is weak,  $N$  is equal to 1.

Next, it should be noted that the accuracy of fitting the WL depends on the magnetic field scale. Specifically,  $L_\phi$  is determined by the curvature of the MR near zero field, while  $L_e$  is determined by the larger field scale  $B_e = \hbar/(2eL_e^2)$ , where the WL disappears completely [2]. We observe a positive MR background at large magnetic field (consistent with the observations in former studies [15,16]) that we attribute to the strong localization effect [19]. The presence of this background limits the magnetic field range that we consider for the fits. As a result,  $B_e$  cannot be accurately determined, so we determine  $L_e$  from the zero-field conductivity and use the phase coherence term as the only fitting parameter to extract  $L_\phi$ . We select the MR section with the strongest curvature near zero field (where both SOC and elastic scattering play a minor role) with a scale  $B_\phi = \hbar/(4eL_\phi^2)$  [see Fig. 2(a)] and fix  $L_e = \sigma \hbar/e^2 \sqrt{4\pi/(g_v n_s)}$  with each  $n_s$  for the fitting. Several examples of our fitting curves are shown in Fig. 2(b). As  $n_s$  increases from  $3.3 \times 10^{12} \text{ cm}^{-2}$  (lower band) to  $4.3 \times 10^{12} \text{ cm}^{-2}$  (upper band), there is a prominent increase of the slope at the field range within  $B_\phi$ , revealing a general trend that  $L_\phi$  increases with  $n_s$ .

We then plot the calculated  $L_e$  and extracted  $L_\phi$  from the HLN model as a function of  $n_s$ . As shown in Fig. 2(c), both  $L_\phi$  and  $L_e$  present a positive correlation with  $n_s$ . In the double-band regime, we compare the estimated values of  $L_\phi$  with  $N$  equal to 1 and 2 (for degenerate double bands), where qualitatively good fits are obtained in both cases for the carrier density dependence, despite marginal differences in the extracted  $L_\phi$ . Also, the two subbands are not degenerate due to the SOC. Once the upper spin-split band is populated, additional scattering sources such as intravalley scattering are involved. In such case,  $N$  should be less than 2 but the exact value is unknown. Therefore, in the following text, we keep the value of  $N$  equal to 1 for the consistency of our fitting. Certain limitations of our model for the double-band regime will be drawn at the end of the section.  $L_\phi$  increases from  $\sim 60 \text{ nm}$  at  $n_s = 3.3 \times 10^{12} \text{ cm}^{-2}$  to  $\sim 105 \text{ nm}$  at  $n_s = 7.4 \times 10^{12} \text{ cm}^{-2}$ , which is among the largest reported for MoS<sub>2</sub> [15–18]. This is attributed to a higher sample quality, as confirmed by the large electron mobility  $\mu = 2300 \text{ cm}^2/\text{Vs}$  [19]. The ratio of the coherence length over mean free path ( $L_\phi/L_e$ ) decreases from above 4.0 at  $n_s < 3.6 \times 10^{12} \text{ cm}^{-2}$  to below 2.0 at  $n_s > 6.3 \times 10^{12} \text{ cm}^{-2}$ , where the WL peak disappears. Indeed, the WL effect is expected to disappear if the coherence length is on the order of the scattering length. In Fig. 2(d), we test the role of the displacement field on the phase coherence length. The displacement field can be used to tune the SOC strength in material with an in-plane SOC such as Rashba [22,23]. However, in our case, the displacement field plays a minor role in both  $L_\phi$  and  $L_e$  at fixed  $n_s$  in both single-band and double-band regimes. The weak tunability by the displacement field suggests that extrinsic (Rashba-type) SOC, if present, plays only a marginal role.

We finally investigate the dephasing mechanism by fitting the  $L_\phi$  as a function of temperature. Figure 3(a) shows the temperature dependence of  $\Delta\sigma(B)$  at  $n_s = 3.0 \times 10^{12} \text{ cm}^{-2}$ . As temperature increases from 1.3 to 5.0 K, an obvious decrease of the slope of  $\Delta\sigma(B)$  within the interval  $|B| < B_\phi$  is observed due to the reduced  $L_\phi$ , whereas  $L_e$  remains roughly constant in the temperature range considered in our experiment

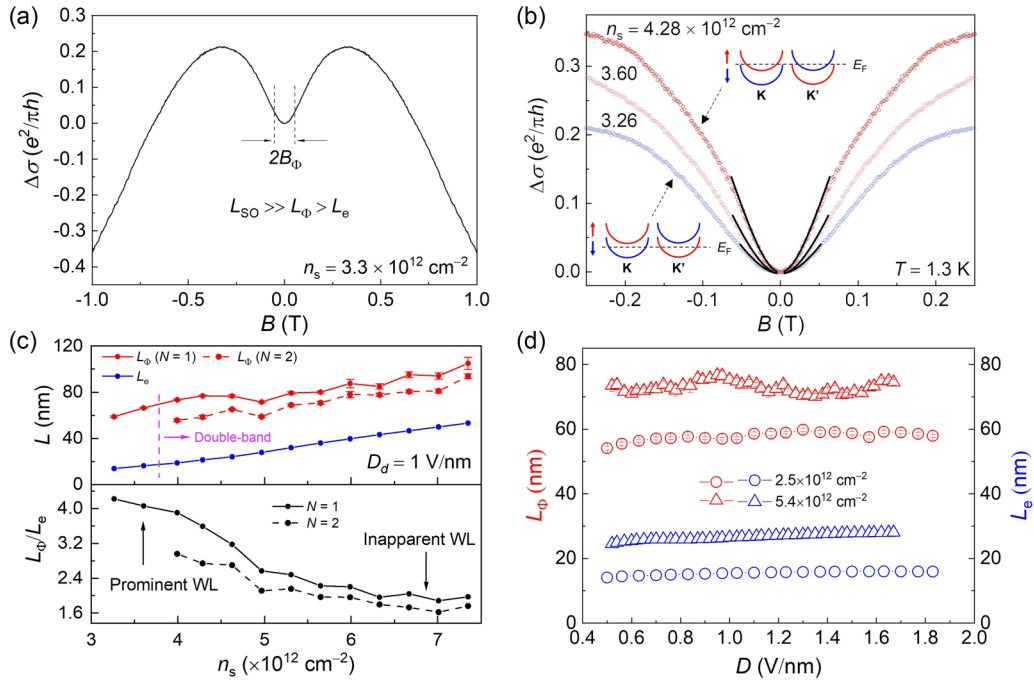


FIG. 2. (a) Symmetrized magnetoconductivity  $\Delta\sigma(B)$ , where  $\Delta\sigma(B) = [\sigma(B) + \sigma(-B)]/2 - \sigma(B = 0 \text{ T})$ , in unit of  $e^2/\pi h$  at  $n_s = 3.3 \times 10^{12} \text{ cm}^{-2}$  and  $T = 1.3 \text{ K}$ . The phase coherence field ( $B_\phi$ ) is scaled in the region with the strongest curvature. (b) Examples about the fitting of  $\Delta\sigma(B)$  curves for both the single-band and double-band regimes. The black lines at the range of  $B_\phi$  are the fits using our redefined HLN model. (c) Top subfigure:  $L_\phi$  and  $L_e$  as a function of  $n_s$ . The dashed line represents the fitting result with  $N$  equal to 2 in the double band regime as the lower limit for the extracted  $L_\phi$ . Bottom subfigure:  $L_\phi/L_e$  as a function of  $n_s$ . Data measured at fixed  $D_d = 1 \text{ V/nm}$  and  $T = 1.3 \text{ K}$ . (d)  $L_\phi$  and  $L_e$  as a function of  $D_d$  at  $n_s = 2.5 \times 10^{12} \text{ cm}^{-2}$  (single band) and  $n_s = 5.4 \times 10^{12} \text{ cm}^{-2}$  (double bands), measured at  $T = 1.3 \text{ K}$ . The error bars in (c) and (d) are measured by a confidence interval of 99.7%.

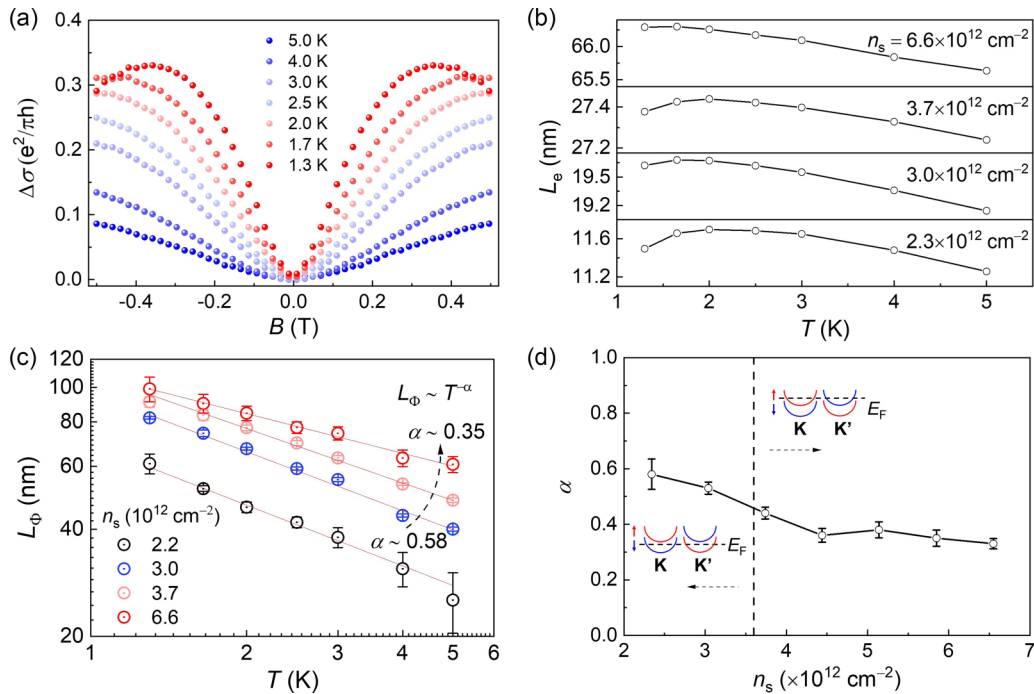


FIG. 3. (a)  $\Delta\sigma(B)$  curves at different temperatures (from 1.3 to 5.0 K) in the lower band regime. (b)  $L_e$ - $T$  curves at different  $n_s$  from  $2.3 \times 10^{12} \text{ cm}^{-2}$  (lower band) to  $6.6 \times 10^{12} \text{ cm}^{-2}$  (upper band). (c)  $L_\phi$ - $T$  curves at different  $n_s$ . The red solid lines are the fits using  $L_\phi \sim T^{-\alpha}$ . (d) The extracted  $\alpha$  as a function of  $n_s$ .

[see Fig. 3(b)]. A weak temperature dependence of  $L_e$  is expected when the resistance is dominated by impurity scattering. The slight decreasing trend with increased temperature for all  $n_s$  is attributed to the metallic phase of MoS<sub>2</sub>. In most cases, the  $L_e$ - $T$  curve appears to be nonmonotonic at  $T < 2$  K. In fact, such an effect is more prominent the lower the density ( $n_s \leq 3.6 \times 10^{12}$  cm<sup>-2</sup>), which hints at other spurious effects such as strong localization. Figure 3(c) depicts the  $L_\phi$ - $T$  curves at different  $n_s$ , which can fit into a power law in the form of  $L_\phi \propto T^{-\alpha}$ , where  $\alpha$  is a constant that depends on the dephasing mechanism. We find that  $\alpha$  is close to 0.5 when only the lower spin-orbit split band ( $K \uparrow$ ,  $K' \downarrow$ ) is occupied, whereas it decreases to around 0.35 when also the upper band ( $K \uparrow$ ,  $K' \downarrow$ ) is filled with electrons [as shown in Fig. 3(d)]. In the low carrier density regime, the  $\alpha$  estimated by our fitting approach hints towards  $e$ - $e$  interaction as the main source of decoherence [24]. In the higher carrier density regime, our model is mainly limited by three factors. First, the exact number of channels (or value of  $N$ ) in our fitting model is unknown because of the two nondegenerate spin-split bands. Second, additional dephasing sources such as intervalley scattering might play a role on the estimated value of  $L_\phi$ . Third, the change of the scale in  $L_\phi$  from 1.5 to 5.0 K is not large enough to extract the precise value of  $\alpha$ . Though the exact scattering mechanism cannot be extracted, our fitting shows a reasonable estimation of  $L_\phi$  (up to 100 nm) and reveals a spin relaxation time much longer than the coherence time. Our result suggests that the spins are well preserved despite several possible scattering events (e.g., Coulomb interaction, intravalley scattering) in atomically thin MoS<sub>2</sub>.

### III. CONCLUSION

In summary, we study weak localization with reliable control of the carrier population in different spin-split bands in a dual-gated bilayer MoS<sub>2</sub>. We did not observe weak antilocalization in the attainable carrier density range. This is attributed to the pronounced intrinsic spin-orbit coupling in MoS<sub>2</sub>, which gives rise to a spin relaxation length much longer than the mean free path and the coherence length, in agreement with the reported long-lived spin relaxation in MoS<sub>2</sub>. Therefore, awareness should be warranted that HLN model cannot reliably estimate the spin relaxation length only in the presence of weak localization. Nevertheless, our model can be expanded close to zero field to estimate the phase coherence length. From our analysis, we could extract phase coherence lengths of the order 100 nm, in agreement with previous publications. At low densities, when only the lower spin-orbit split bands are occupied, the coherence length is limited by electron-electron scattering.

### ACKNOWLEDGMENTS

We thank S. Iwakiri and Z. Lei for fruitful discussions. We thank P. Märki, T. Bähler, as well as the FIRST staff for their technical support. T.I. and K.E. acknowledge support from the European Graphene Flagship Core3 Project, Swiss National Science Foundation via NCCR Quantum Science, and H2020 European Research Council (ERC) Synergy Grant under Grant Agreement No. 95154. B.O. acknowledges the

support from the Singapore NRF Investigatorship (Grant No. NRF-NRFI2018-8), Competitive Research Programme (Grant No. NRF-CRP22-2019-8), and MOE-AcRF-Tier 2 (Grant No. MOE-T2EP50220-0017). K.W. and T.T. acknowledge support from JSPS KAKENHI (Grants No. 19H05790, No. 20H00354, and No. 21H05233).

### APPENDIX A: DEVICE FABRICATION AND MEASUREMENTS

First, we assemble the bottom hBN (as the bottom dielectric layer) and graphite flake (as the bottom gate) onto a Si/SiO<sub>2</sub> substrate (with 285-nm-thick oxide layer), using a standard dry-transfer method [7]. We then pattern metallic contacts (made by Cr/Au: 5 nm/10 nm) through standard electron beam lithography and electron beam evaporation. The residuals on the contact regions (due to lithography process) are then thoroughly cleaned by the tip of an atomic force microscope in contact mode. Next, we identify the bilayer MoS<sub>2</sub>. We employ the mechanical exfoliation from bulk MoS<sub>2</sub> crystals (obtained from SPI Supplies) onto a Si/SiO<sub>2</sub> substrate (with 285-nm-thick oxide layer) and then identify the bilayer by its optical contrast, with a highly reliable method [25,26]. Then, we assemble the second stack containing the top hBN (as the top dielectric layer) and the selected bilayer MoS<sub>2</sub>. This stack is aligned and transferred onto the contacts. The transfer is performed in a glove box with an argon atmosphere, ensuring minimal exposure to H<sub>2</sub>O and O<sub>2</sub> (both <0.1 ppm). Finally, a metallic top gate (that covers the entire MoS<sub>2</sub> flake) is patterned using standard electron beam lithography and electron beam evaporation. The final stack is annealed in vacuum condition at 250 °C for 4 h to reduce the bubbles and improve the quality of the contact interface. The thicknesses for the bottom and top hBN layers are determined by atomic force microscopy in tapping mode, which yields  $d_B = 13$  nm and  $d_T = 20$  nm, respectively. The device information is shown in Fig. 4.

According to a parallel plate capacitor model ( $C = \epsilon\epsilon_0/d$ ), the thickness  $d_B$  ( $d_T$ ) yields the capacitance per area  $C_B = 225$  nF/cm<sup>2</sup> ( $C_T = 146$  nF/cm<sup>2</sup>). These values are used in the main text to determine the electron density as a function of bottom and top gate voltages. The capacitance per area obtained by the parallel plate capacitor model is then confirmed experimentally by measuring the electron density from the SdH oscillations [see Fig. 2(b) of Ref. [19] for a direct comparison].

The measurements are performed by lock-in techniques (with excitation voltage at 100  $\mu$ V and frequency at  $\sim 30$  Hz). The temperature range is 1.3–10 K and magnetic-field range is 0–7 T.

### APPENDIX B: SIMULATION ON THE TURNOVER FROM WL TO WAL

The general form for weak location in thin films can be written by [1]

$$\sigma(H) = -\frac{e^2}{2\pi^2 h} \left[ \Psi\left(\frac{1}{2} + \frac{B_1}{B}\right) - \Psi\left(\frac{1}{2} + \frac{B_2}{B}\right) + \frac{1}{2} \Psi\left(\frac{1}{2} + \frac{B_3}{B}\right) - \frac{1}{2} \Psi\left(\frac{1}{2} + \frac{B_4}{B}\right) \right],$$

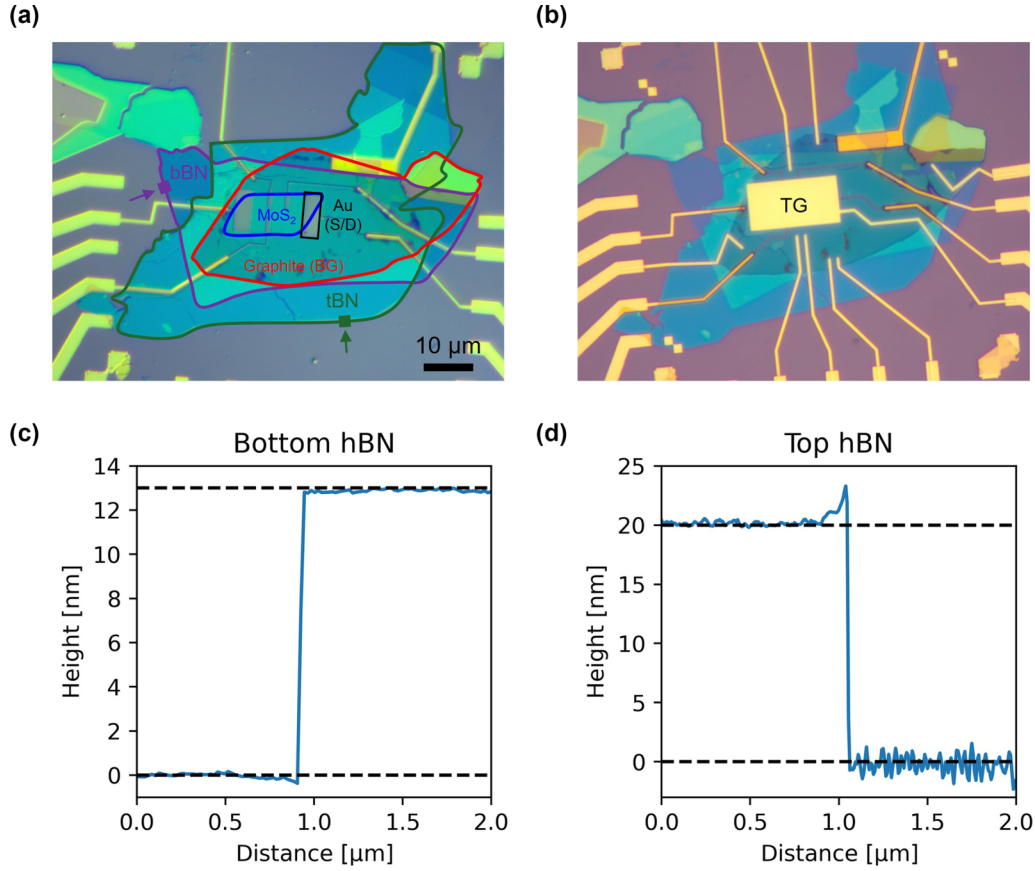


FIG. 4. (a) Optical micrograph of the stack without the top gate (TG). A multilayer graphite (outlined by the red line) acts as the back gate (BG); the bottom BN (bBN, outlined by the red line) acts as bottom dielectric layer; the bilayer MoS<sub>2</sub> (outlined by the blue line) is probed by Au contacts (one outlined by the black line); the top BN (tBN, outlined by the purple line) acts as the top dielectric layer. (b) Optical micrograph of the stack after forming the top gate. (c) Thickness profile ( $\sim 13.5$  nm) of the bottom hBN flake (in the region denoted by the purple box) measured by atomic force microscopy. (d) Thickness profile ( $\sim 20$  nm) of the top hBN flake (in the region denoted by the green box) measured by atomic force microscopy.

where

$$B_1 = B_o + B_{so} + B_s,$$

$$B_2 = \frac{4}{3}B_{so} + \frac{2}{3}B_s + B_i,$$

$$B_3 = 2B_s + B_i,$$

$$B_4 = \frac{4}{3}B_{so} + \frac{2}{3}B_s + B_i.$$

The terms  $o$ ,  $i$ ,  $s$ , and  $SO$  in the above formulae refer to potential scattering (for mean free path), inelastic scattering (for phase decoherence), magnetic scattering, and spin-orbit scattering (for spin relaxation related to spin-orbit coupling), respectively.  $\Psi$  is the digamma function.

In pristine MoS<sub>2</sub>, the magnetic scattering should be left out, leading to the Hikami-Larkin-Nagaoka (HLN) model that includes the spin-orbit term, phase-coherence term, and elastic-scattering term in the form

$$\Delta\sigma(B) = \frac{e^2}{2\pi h} \left[ \ln\left(\frac{B_\phi}{B}\right) - \Psi\left(\frac{1}{2} + \frac{B_\phi}{B}\right) \right] + \frac{e^2}{\pi h} \left[ \ln\left(\frac{B_{so} + B_e}{B}\right) - \Psi\left(\frac{1}{2} + \frac{B_{so} + B_e}{B}\right) \right]$$

$$+ \frac{3e^2}{2\pi h} \left[ -\ln\left(\frac{4/3B_{so} + B_\phi}{B}\right) + \Psi\left(\frac{1}{2} + \frac{4/3B_{so} + B_\phi}{B}\right) \right],$$

where  $B_{so}$ ,  $B_\phi$ ,  $B_e$  refer to the field scales for the spin-orbit coupling, phase coherence, and elastic scattering, respectively.  $\Delta\sigma(B) = [\sigma(B) + \sigma(-B)]/2 - \sigma(B=0 \text{ T})$  represents the normalized conductivity in the unit of  $e^2/\pi h$ .

$\sigma(B)$  can be calculated by the Drude model through the following relations:

$$\sigma_{xx}(B) = \rho_{xx}(B)/(\rho_{xx}^2(B) + \rho_{xy}^2(B)),$$

where  $\rho_{xx}$  and  $\rho_{xy}$  represent the longitudinal and transverse resistivities, respectively. In 2D systems,  $\rho_{xx(xy)}$  is given by

$$\rho_{xx(xy)} = R_{xx(xy)} \frac{W}{L},$$

where  $R_{xx}$  and  $R_{xy}$  represent the longitudinal and transverse resistances, respectively.  $W$  and  $L$  are the width ( $8.5 \mu\text{m}$ ) and length ( $3.0 \mu\text{m}$ ) of the characterized channel in MoS<sub>2</sub>.

$B_{so}$ ,  $B_\phi$ , and  $B_e$  can be determined by the spin-relaxation length ( $L_{so}$ ), phase coherence length ( $L_\phi$ ), and mean free path

( $L_e$ ), respectively:

$$B_{SO} = \hbar/(4eL_{SO}^2),$$

$$B_\phi = \hbar/(4eL_\phi^2),$$

$$B_e = \hbar/(2eL_e^2).$$

$L_\phi$  is extracted by the fitting the WL shown in the main text, and  $L_e$  can be calculated by  $L_e = \sigma(B = 0 \text{ T})\hbar/e^2\sqrt{4\pi/(g_v n_s)}$ , where  $g_v = 2$  is the valley degeneracy in each spin-valley locked band and  $n_s$  is total carrier density. At  $n_s = 3.3 \times 10^{12} \text{ cm}^{-2}$ , we obtain  $L_\phi = 60 \text{ nm}$  ( $B_\phi = 0.05 \text{ T}$ ) and  $L_e = 14 \text{ nm}$  ( $B_e = 0.84 \text{ T}$ ).

We then simulate how the SOC plays a role on the turnover from WL to WAL. We choose a range of  $B_{SO}$  for the modeling and obtain the simulation curves in Fig. 5, where a turnover from WL to WAL can be observed. The turning point corresponds to  $L_{SO} \cong 109 \text{ nm}$ . This means that in the single-band regime of MoS<sub>2</sub>, the spin relaxation is rather long ( $L_{SO} \gg L_\phi > L_e$ ).

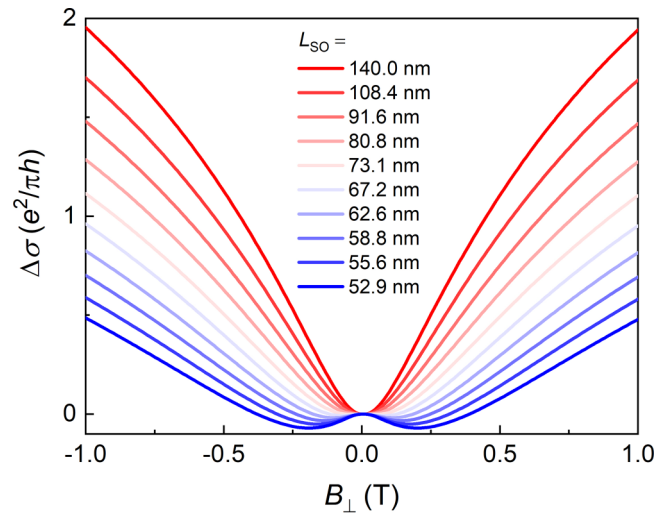


FIG. 5. Simulation on the turnover from WL to WAL by tuning the SOC in the single-band regime in MoS<sub>2</sub>.

- [1] G. Bergmann, Weak localization in thin films: A time-of-flight experiment with conduction electrons, *Phys. Rep.* **107**, 1 (1984).
- [2] T. Ihn, *Semiconductor Nanostructures: Quantum States and Electronic Transport* (Oxford University Press, Oxford, 2009).
- [3] S. Manzeli, D. Ovchinnikov, D. Pasquier, O. V. Yazyev, and A. Kis, 2D transition metal dichalcogenides, *Nat. Rev. Mater.* **2**, 1 (2017).
- [4] Z. Y. Zhu, Y. C. Cheng, and U. Schwingenschlögl, Giant spin-orbit-induced spin splitting in two-dimensional transition-metal dichalcogenide semiconductors, *Phys. Rev. B* **84**, 153402 (2011).
- [5] D. Xiao, G. B. Liu, W. Feng, X. Xu, and W. Yao, Coupled spin and valley physics in monolayers of MoS<sub>2</sub> and other group-VI dichalcogenides, *Phys. Rev. Lett.* **108**, 196802 (2012).
- [6] R. Suzuki, M. Sakano, Y. J. Zhang, R. Akashi, D. Morikawa, A. Harasawa, K. Yaji, K. Kuroda, K. Miyamoto, T. Okuda, K. Ishizaka, R. Arita, and Y. Iwasa, Valley-dependent spin polarization in bulk MoS<sub>2</sub> with broken inversion symmetry, *Nat. Nanotechnol.* **9**, 611 (2014).
- [7] R. Pisoni, T. Davatz, K. Watanabe, T. Taniguchi, T. Ihn, and K. Ensslin, Absence of interlayer tunnel coupling of K-valley electrons in bilayer MoS<sub>2</sub>, *Phys. Rev. Lett.* **123**, 117702 (2019).
- [8] M. Masseroni, T. Davatz, R. Pisoni, F. K. de Vries, P. Rickhaus, T. Taniguchi, K. Watanabe, V. Fal'ko, T. Ihn, and K. Ensslin, Electron transport in dual-gated three-layer MoS<sub>2</sub>, *Phys. Rev. Res.* **3**, 023047 (2021).
- [9] S. Hikami, A. I. Larkin, and Y. Nagaoka, Spin-orbit interaction and magnetoresistance in the two-dimensional random system, *Prog. Theor. Phys.* **63**, 707 (1980).
- [10] G. Bergman, Influence of spin-orbit coupling on weak localization, *Phys. Rev. Lett.* **48**, 1046 (1982).
- [11] H. Ochoa, F. Finocchiaro, F. Guinea, and V. I. Fal'ko, Spin-valley relaxation and quantum transport regimes in two-dimensional transition-metal dichalcogenides, *Phys. Rev. B* **90**, 235429 (2014).
- [12] S. Ilić, J. S. Meyer, and M. Houzet, Weak localization in transition metal dichalcogenide monolayers and their heterostructures with graphene, *Phys. Rev. B* **99**, 205407 (2019).
- [13] S. McPhail, C. E. Yasin, A. R. Hamilton, M. Y. Simmons, E. H. Linfield, M. Pepper, and D. A. Ritchie, Weak localization in high-quality two-dimensional systems, *Phys. Rev. B* **70**, 245311 (2004).
- [14] A. Zduniak, M. I. Dyakonov, and W. Knap, Universal behavior of magnetoconductance due to weak localization in two dimensions, *Phys. Rev. B* **56**, 1996 (1997).
- [15] H. Schmidt, I. Yudhistira, L. Chu, A. C. Neto, B. Özyilmaz, S. Adam, and G. Eda, Quantum transport and observation of Dyakonov-Perel spin-orbit scattering in monolayer MoS<sub>2</sub>, *Phys. Rev. Lett.* **116**, 046803 (2016).
- [16] N. Papadopoulos, K. Watanabe, T. Taniguchi, H. S. Van Der Zant, and G. A. Steele, Weak localization in boron nitride encapsulated bilayer MoS<sub>2</sub>, *Phys. Rev. B* **99**, 115414 (2019).
- [17] A. T. Neal, H. Liu, J. Gu, and P. D. Ye, Magneto-transport in MoS<sub>2</sub>: Phase coherence, spin-orbit scattering, and the hall factor, *ACS Nano* **7**, 7077 (2013).
- [18] Y. J. Zhang, W. Shi, J. T. Ye, R. Suzuki, and Y. Iwasa, Robustly protected carrier spin relaxation in electrostatically doped transition-metal dichalcogenides, *Phys. Rev. B* **95**, 205302 (2017).
- [19] M. Masseroni, T. Qu, T. Taniguchi, K. Watanabe, T. Ihn, and K. Ensslin, Evidence of the coulomb gap in the density of states of MoS<sub>2</sub>, *Phys. Rev. Res.* **5**, 013113 (2023).
- [20] H. Ochoa and R. Roldán, Spin-orbit-mediated spin relaxation in monolayer MoS<sub>2</sub>, *Phys. Rev. B* **87**, 245421 (2013).
- [21] L. Yang, N. A. Sinitsyn, W. Chen, J. Yuan, J. Zhang, J. Lou, and S. A. Crooker, Long-lived nanosecond spin relaxation and

- spin coherence of electrons in monolayer MoS<sub>2</sub> and WS<sub>2</sub>, *Nat. Phys.* **11**, 830 (2015).
- [22] K. Premasiri, S. K. Radha, S. Sucharitakul, U. R. Kumar, R. Sankar, F. Chou, Y. Chen, and X. P. A. Gao, Tuning Rashba spin-orbit coupling in gated multilayer InSe, *Nano Lett.* **18**, 4403 (2018).
- [23] T. Koga, J. Nitta, T. Akazaki, and H. Takayanagi, Rashba spin-orbit coupling probed by the weak antilocalization analysis in InAlAs/InGaAs/InAlAs quantum wells as a function of quantum well asymmetry, *Phys. Rev. Lett.* **89**, 046801 (2002).
- [24] B. L. Altshuler, A. G. Aronov, and D. E. Khmel'nitsky, Effects of electron-electron collisions with small energy transfers on quantum localisation, *J. Phys. C: Solid State Phys.* **15**, 7367 (1982).
- [25] H. Li, G. Lu, Z. Yin, Q. He, H. Li, Q. Zhang, and H. Zhang, Optical identification of single- and few-layer MoS<sub>2</sub> sheets, *Small* **8**, 682 (2012).
- [26] D. Bing, Y. Wang, J. Bai, R. Du, G. Wu, and L. Liu, Optical contrast for identifying the thickness of two-dimensional materials, *Opt. Commun.* **406**, 128 (2018).